JOURNAL OF
SYNCHROTRON
RADIATION

ISSN 1600-5775

# A micro-focusing and high-flux-throughput beamline design using a bending magnet for microscopic XAFS at the High Energy Photon Source

**Kun Tang,* Lei Zheng, Yi Dong Zhao, Shu Hu Liu, Chen Yan Ma and Yu Hui Dong**

Institute of High Energy Physics, 19B Yuquan Road, Shijingshan District, Beijing, People's Republic of China.
*Correspondence e-mail: tangk@ihep.ac.cn

Received 1 February 2019
Accepted 16 May 2019

Edited by I. Lindau, SLAC/Stanford University, USA

**Keywords:** bending-magnet beamline; micro-XAFS; full-field nano-XAFS; full-field transmission X-ray microscopy; quick-XAFS; HEPS; XAFS.

An optical design study of a bending-magnet beamline, based on multi-bend achromat storage ring lattices, at the High Energy Photon Source, to be built in Beijing, China, is described. The main purpose of the beamline design is to produce a micro-scale beam from a bending-magnet source with little flux loss through apertures. To maximize the flux of the focal spot, the synchrotron source will be 1:1 imaged to a virtual source by a toroidal mirror; a mirror pair will be used to collimate the virtual source into quasi-parallel light which will be refocused by a Kirkpatrick–Baez mirror pair. In the case presented here, a beamline for tender X-rays ranging from 2.1 keV to 7.8 keV, with a spot size of approximately 7 µm (H) × 6 µm (V) and flux up to $2 \times 10^{12}$ photons $s^{-1}$, can be achieved for the purpose of X-ray absorption fine-structure (XAFS)-related experiments, such as scanning micro-XAFS and full-field nano-XAFS.

## 1. Introduction

The High Energy Photon Source (HEPS), a 6 GeV diffraction-limited, ∼34.2 pm rad storage-ring light source, is under construction in Beijing, China, and will be operational before 2025 (Jiao *et al.*, 2018). The HEPS storage ring comprises 48 7BA cells that are grouped in 24 super-periods, each consisting of two straight sections and two bending magnets that can be used as sources. The overall planning goal of the HEPS comprises more than 90 beamlines, with 14 carried out in Phase I, including a bending-magnet beamline for X-ray absorption fine-structure (XAFS) applications with tender X-rays, which is presented here.

XAFS is a powerful technique to investigate local atomic geometry and the chemical state of the atoms of one specific element in almost any type of substance. XAFS beamlines (Welter, 2012) have been constructed in almost every synchrotron radiation facility for a wide range of applications, including physics, chemistry, geology, environmental science and energy materials. Two XAFS beamlines are to be built in Phase I of the HEPS, one for a broad energy range of 5 keV–40 keV based on an undulator, and the other a bending-magnet beamline for an energy range of 2.1 keV–7.8 keV to cover the energy gap missing from the undulator beamline. Within this energy range, the *K*-edges of elements from phosphorus to cobalt are accessible, and the *L*-edges of the elements from strontium to gadolinium can be studied. The beamline for tender X-ray XAFS applications will provide at least two stations, one for bulk-size (∼mm) samples with a general purpose, and the other for micro-size (20 nm–100 µm)

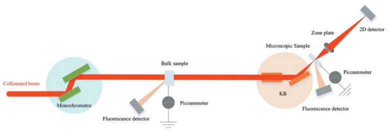

https://doi.org/10.1107/S160057751900715X

samples based on a microprobe or microscope. XAFS with spatial resolution is clearly useful to study inhomogeneous samples or particles that have a micro-spatial structure. Such a method can be called microscopic XAFS (Guttmann *et al.*, 2012; Meirer & Weckhuysen, 2018) or, depending on the spatial resolution, micro- (Silversmit *et al.*, 2009) or nano-XAFS (Meirer *et al.*, 2011).

There are two main types of synchrotron-based X-ray microscopic XAFS (Falcone *et al.*, 2011). One is the scanning mode (Barrea *et al.*, 2010) and the other is full-field X-ray transmission mode (Meirer *et al.*, 2011). In scanning mode, a sample is scanned in the focal plane, often with a spatial resolution of 10 nm to 10 µm, which equals the size of the focus. Either fluorescence, transmission X-rays or photoelectrons can be used as a diagnostic signal. The main drawback to obtaining an XAFS image is that the collection time is the product of the quick-XAFS interval and the number of two-dimensional pixels, which is huge. Furthermore, it is difficult to design a beamline to obtain a spatial resolution of less than 0.5 µm without losing flux due to many restrictions, including the emittance of the source, the diffraction of photons, the cutoff incidence angle of coatings and the slope error of optical elements. As a result, a sub-micro-size focus often means a low flux and a small field of view (FOV) for scanning.

Full-field XAFS is based on an X-ray transmission microscope (TXM) (Jefimovs *et al.*, 2008; Guttmann *et al.*, 2012). The FOV of a TXM is the size of the focus, which will be imaged to a detector plane at the same time (Meirer *et al.*, 2011). Obviously, full-field XAFS can reduce the acquisition time for an image. The spatial resolution, which mainly depends on the outermost zone width of a Fresnel zone plate (FZP) used as an objective lens, is often approximately 20 nm–50 nm. However, it is difficult to achieve the divergence a TXM requires. The divergence of the focus should be comparable with the acceptances of the FZP in both the horizontal and vertical planes, often in the range 2–5 mrad. A large divergence often means a better spatial resolution (Vila-Comamala *et al.*, 2012), whereas a large focus beam size often means a large FOV. The phase space, which is the product of the beam size of the focus and the divergence of the focus, is used as a specification for TXM applications, and is often not less than 20 µm mrad in both directions.

Theoretically and ideally, the beam phase space based on an undulator is the convolution of the emittance of electron bunches and the natural emittance of photons, especially at the HEPS. Unfortunately, the emittance of 34.2 pm rad at the HEPS is far from the value of the phase space demanded by an application of TXM-based nano-XAFS. As a result, if using an undulator as a source, which is diffraction-limited, it is necessary to drastically increase the beam phase space. There are many ways to accomplish this. The most conventional ways are to use the slope error of mirrors to increase it and apertures to reduce it. The diffraction and aberration of optics can also be used to increase the phase space. However, diffraction and apertures are often used at the expense of flux, and to use slope error or aberration may cause modulation of the intensity distribution.

For example, if using an undulator as a source that is close to the emittance of the ring, a condenser in the form of a beam-shaping FZP (Jefimovs *et al.*, 2008; Winarski *et al.*, 2012), with an average diffraction efficiency of 7%, is often used to drastically increase the beam phase space. The most notable advantage of using a beam-shaping FZP, which is essentially a diffractive optical element with a deliberately deteriorating aberration, is that it can produce a square-shaped, intense, flat-top illumination which is well matched to the detector. The drawback of using a beam-shaping FZP is that an optical element depending on energy is not favorable for successive energy scanning applications. Using a Kirkpatrick–Baez (KB) mirror (Rau *et al.*, 2006) as a condenser can solve this problem, and it can also reduce the flux loss, as demonstrated in some beamlines based on undulators. The main problem with a KB condenser is that the FOV is small if the divergence is large. A single-bounce capillary (Barrea *et al.*, 2009; Winarski *et al.*, 2012), which is essentially an ellipsoidal mirror with a much larger slope error compared with KB, can be used to drastically expand the phase space. However, a capillary only uses the outer ring of the beam, often with a transmission of approximately 25%. In summary, all these methods have flaws if an inappropriate source is used for TXM-related applications.

If using a bending magnet or wiggler (Lee *et al.*, 2015) as the source for nano-XAFS, the beam phase space will be much closer to the requirements of such a method, even though at the HEPS only vertical phase space must be expanded. However, despite a relatively appropriate phase space, a condenser which is often a capillary must still be used to expand the inappropriate divergence in a conventional design (Andrews *et al.*, 2009). Furthermore, due to the difference of divergence in two directions, most flux is lost during the process, which is a transformation of phase space. The total transmission of flux is low, and the flux for TXM-related applications based on a conventional bending-magnet design is often on the order of $1 \times 10^9$ photons $s^{-1}$ (Tian *et al.*, 2008; Yuan *et al.*, 2012; Wang *et al.*, 2018).

Therefore, for the purpose of microscopic XAFS, an optical design study for little flux loss is presented here instead of a conventional design. A design dealing with beams independently in both the horizontal and vertical directions is meant to produce a micro-scale beam from a bending-magnet source, with a flux up to $2 \times 10^{12}$ photons $s^{-1}$ and a proper divergence of 3–5 mrad. In addition to the advantage of thermal stability and the convenience of energy scanning, the greatest advantage of this design is that the flux can be of the order of $1 \times 10^{12}$ photons $s^{-1}$, for either micro-XAFS or TXM-based nano-XAFS. Details are provided below.

## 2. Source

Due to the large number of beamlines planned at the HEPS, there is insufficient space to put a long mirror in the tunnel. As a result, the first mirror can only be placed outside the tunnel at a position of 33.5 m, which is the shortest distance between the source and a long mirror in the vacuum chamber that can

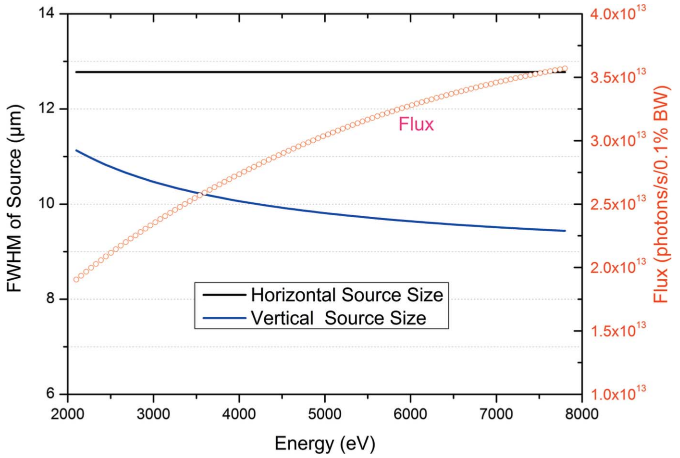

**Figure 1**
Assuming the emittance of the ring is 34.2 pm rad, *βx* is 0.4654 m, *βy* is 3.751 m, the acceptance is 1.7 mrad (H) × 0.2 mrad (V), the magnetic field is 1 T and the ring current is 200 mA; the green curve represents the source size in the vertical direction, while the black curve represents the source size in the horizontal direction. The red dotted curve represents the flux of the source.

be achieved. To receive more flux from the source, a long mirror with an active optical length of 1 m will be used, which corresponds to a receiving aperture of approximately 1.7 mrad (H) × 0.2 mrad (V).

To minimize some unfavorable effects on the storage ring, all bending magnets for sources at the HEPS will work under a magnetic field of 1 T at the present stage, at least until Phase II. The values of the *β* functions of the bending magnet are 0.4654 m and 3.751 m in the horizontal and vertical directions, respectively. The flux and full width at half-maximum (FWHM) of the source size were calculated using *Spectra* code (Tanaka & Kitamura, 2001), assuming a ring current of 200 mA. These results are shown in Fig. 1. The flux can be further improved in the future if using an appropriate magnetic field of the source.

The beam phase space can be calculated according to Fig. 1 by multiplying the size by the divergence, approximately 22 μm mrad (H) and 2 μm mrad (V), respectively.

## 3. Optical layout of beamline for tender X-rays

The goal of this design is generally to make the most of the very small size of the source to achieve a micro-beam with a maximized flux. Five mirrors, including a toroidal mirror (TM) for the virtual source, a mirror pair (CHKB, CM) for collimating and a KB mirror pair (HKB, VKB) for focusing, are used for this purpose. A schematic of the beamline is shown in Fig. 2.

The TM deflects the beam in the vertical direction, focusing the source along both the horizontal and vertical directions with 1:1 demagnification. Under this demagnification, the aberration of optics is minimized; the ideal virtual source would be 13 μm (H) × 17 μm (V). However, if we account for the influence of reasonable surface error of approximately 1 μrad and 5 μrad in the tangential and sagittal directions, respectively, the realistic FWHM of the virtual source, which is a function of the image distance and slope error, will be 17 μm (H) × 170 μm (V).

Since a sagittal slope error contributes much less to the focus size than a tangential slope error, the horizontal beam size that inherits the characteristics of the source is much smaller. A simulation performed with *SHADOW*/*XOP* code (Canestrari *et al.*, 2011) is shown in Fig. 3. A broadened phase space is obtained, measuring approximately 29 μm mrad (H) × 34 μm mrad (V).

The quality of the final spot depends on the shape of the virtual source. Research (Moreno *et al.*, 2007) shows that a long-period slope error of the mirror surface, which produces secondary foci, together with the small emittance of the photon source, is the significant factor for the shape of beam. A French industrial design company, IRELEC, based in Saint-Martin-d'Hères, can make a toroidal mirror with an optically active area of 1 m and a slope error of approximately 1.0 μrad to deal with a long-period slope error. A bender (Juanhuix *et al.*, 2014) that can compensate for a long-period slope error or transform it to a short-period slope error by using calibrated and accurate push-and-pull actuators placed in specific positions along the mirror will be helpful for the shape of the virtual source.

The most important part of this design is to generate a virtual source using a TM mirror. Such methods already exist at some beamlines, such as ALS10.3.2 (Yashchuk *et al.*, 2015; Marcus *et al.*, 2004) and NSLS II 4BM. These beamlines have a micrometre-sized beam, but at the expense of massive flux. Because of the multi-bend achromat lattice structure at a diffraction-limited facility such as HEPS, we can make the most of the virtual source in two directions, as shown below.

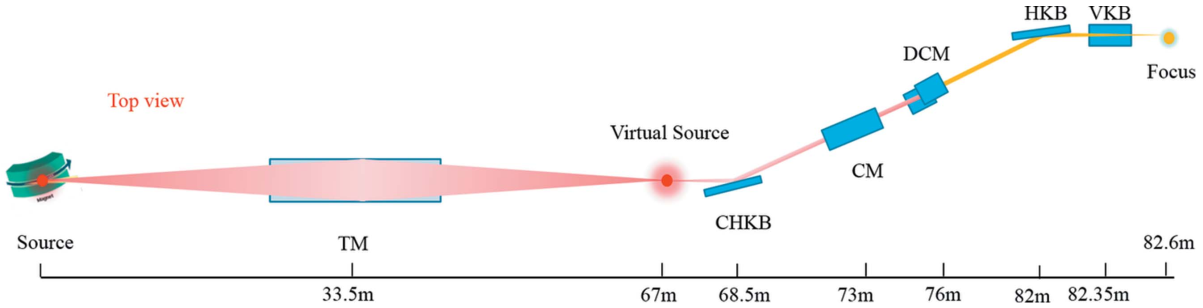

**Figure 2**
Schematic of the bending-magnet beamline at the High Energy Photon Source (HEPS). TM denotes a toroidal mirror; CHKB, HKB and VKB are mirrors shaped in a parabolic cylinder; CM is a cylindrical mirror shaped in the tangential direction; DCM denotes a double-crystal monochromator.

**Table 1**
Optical parameters.

RMS denotes the root mean square and DCM denotes a double-crystal monochromator.

| | TM | CHKB | CM | DCM | HKB | VKB |
|---|---|---|---|---|---|---|
| Position (m) | 33.5 | 68.5 | 73 | 76 | 82 | 82.35 |
| Reflection direction | Upward | Horizontal | Downward | Vertical | Horizontal | Upward |
| Final shape | Toroidal | Parabolic cylinder | Cylindrical | Flat | Parabolic cylinder | Parabolic cylinder |
| Object distance (m) | 33.5 | 1.5 | 6 | – | ∞ | ∞ |
| Image distance (m) | 33.5 | ∞ | ∞ | – | 0.6 | 0.25 |
| Tangential radius (m) | 4785 | ∼462 | 1715 | – | ∼197 | ∼85 |
| Sagittal radius (m) | 0.2345 | – | – | – | – | – |
| Optic active area (L × H) | 1000 × 60 | 400 × 10 | 240 × 20 | | 380 × 10 | 240 × 10 |
| Angle of incidence | 7 mrad | 6.5 mrad | 7 mrad | 14–72° | 6.1 mrad | 5.9 mrad |
| Coating | Ni | Ni | Ni/$B_4C$ | | Ni | Ni |
| Material | Si | Si | Si | Si(111) Si(220) | Si | Si |
| Slope error (μrad RMS) | 1.0/5 | 1.0/5 | 1.0/5 | – | 0.5/5 | 0.5/5 |
| Roughness (nm RMS) | <0.3 | <0.3 | <0.3 | – | <0.3 | <0.3 |

### 3.1. Expected focus and divergence

The next mission is to transform a white virtual source with an FWHM size of 17 μm (H) × 170 μm (V) and a full divergence of 1.7 mrad (H) × 0.2 mrad (V) to a monochromatic micro-spot size while decreasing the phase space as little as possible, which means losing the least flux through apertures.

First, the horizontal divergence angle of the virtual source is so large that it becomes difficult to handle with increasing distance between the virtual source and mirror. To solve this problem, a parabolic cylindrical mirror (CHKB) adjacent to the virtual source is used for collimating in the horizontal direction. The optical structure of collimation and focusing should follow the rules of optical demagnification, and the distance between these two mirrors does not affect the final focus size. Thanks to the 17 μm horizontal virtual source, a micrometre focus does not require great horizontal demagnification.

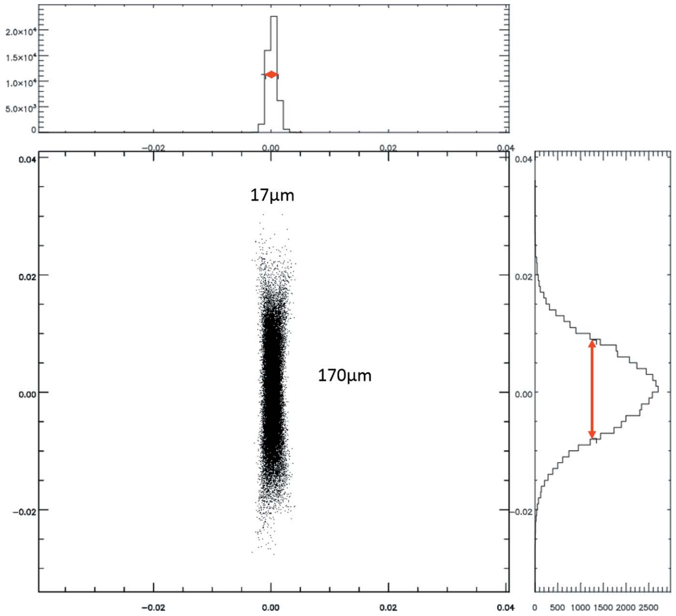

**Figure 3**
Simulation result of the virtual source, assuming the slope errors of the TM are 1 μrad and 5 μrad in the tangential and sagittal directions, respectively. The axis units in the *SHADOW* plots are given in centimetres.

Second, a much larger vertical demagnification is necessary, approximately 10× that in the horizontal direction according to the beam size of the virtual source. Because of the energy range 2.1 keV–7.8 keV, the polarization of the source and the diffraction efficiency of the crystal based on polarization, the crystal should deflect the beam vertically, and is called a vertical monochromator. Moreover, for energy resolution, the optical structure of collimation and focusing should also be used in the vertical direction.

Finally, we choose a demagnification of 2.5 in the horizontal direction and 24 in the vertical direction, collimating and focusing independently, and dealing with beams independently in the horizontal and vertical directions. The optical parameters are shown in Table 1.

The FWHM of the focus beam is approximately 7 μm (H) × 6 μm (V), and the FWHM of this focus beam divergence is approximately 3.6 mrad (H) × 4.5 mrad (V). The simulation result is shown in Fig. 4. The calculation accounts for the influence of the surface error, as shown in Table 1.

The beam between the monochromator and KB can also be useful. The FWHM of this beam size is approximately 2.4 mm (H) × 1.0 mm (V), and the FWHM of the beam divergence is approximately 12 μrad (H) × 28 μrad (V).

### 3.2. Expected flux and energy resolution

The X-ray transmission efficiency and energy resolution of this beamline are calculated by *SHADOW*/*XOP* code. The simulation results are shown in Table 2. Crystal pairs of Si (111) are used to cover the energy range of tender X-rays.

Due to the absorption of the Si (111) crystal, the crystal diffraction efficiency of tender X-rays is less than that of hard X-rays, but a deformed Darwin curve can lead to higher energy resolution as the energy declines. Three pieces of graphenic carbon (Huebner *et al.*, 2015*a*,*b*) window, 900 nm-thick (available from KETEK based in München, Germany), are used to isolate the optical elements and experimental stations. To avoid X-ray absorption of air, there is no air path between source and sample, and sample chambers between

**Table 2**
Expected flux and energy resolution for microscopic XAFS.

The geometric transmission is ~0.8 and the beam size FWHM is ~7 µm (H) × 6 µm (V). 'Diffraction efficiency of double crystals' takes both energy bandwidth and reflectivity of crystals into account, changing the units of flux from photons $s^{-1}$ (0.1% bandwidth)$^{-1}$ to photons $s^{-1}$.

| | 2100 eV | 2500 eV | 3000 eV | 4000 eV | 5000 eV | 6000 eV | 7000 eV | 7800 eV |
|---|---|---|---|---|---|---|---|---|
| Flux of source [photons $s^{-1}$ (0.1% bandwidth)$^{-1}$] | $1.9 \times 10^{13}$ | $2.1 \times 10^{13}$ | $2.3 \times 10^{13}$ | $2.7 \times 10^{13}$ | $3.0 \times 10^{13}$ | $3.2 \times 10^{13}$ | $3.4 \times 10^{13}$ | $3.6 \times 10^{13}$ |
| Transmission of mirrors | 0.64 | 0.67 | 0.67 | 0.72 | 0.73 | 0.73 | 0.69 | 0.53 |
| Diffraction efficiency of double crystals | 0.020 | 0.032 | 0.045 | 0.068 | 0.084 | 0.098 | 0.107 | 0.110 |
| Transmission of windows | 0.84 | 0.90 | 0.94 | 0.97 | 0.98 | 0.99 | 0.99 | 0.99 |
| Flux (photons $s^{-1}$) | $1.6 \times 10^{11}$ | $3.3 \times 10^{11}$ | $5.2 \times 10^{11}$ | $1.0 \times 10^{12}$ | $1.4 \times 10^{12}$ | $1.8 \times 10^{12}$ | $2.0 \times 10^{12}$ | $1.7 \times 10^{12}$ |
| Energy resolution ($E/\Delta E$) | >10000 | >10000 | 9000 | 8500 | 8200 | 7700 | 6800 | 6700 |

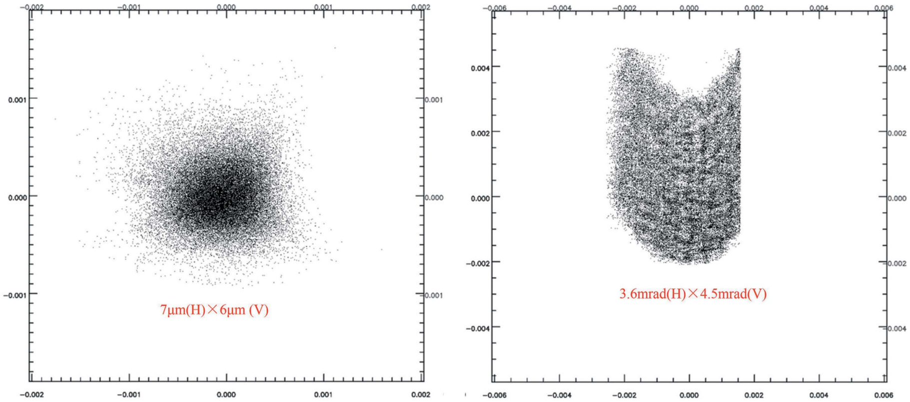

**Figure 4**
*SHADOW* plots of (left) the size of the focus beam (axis units: cm) and (right) the divergence of the focus beam (axis units: rad).

windows are vacuumed or gas-filled with He. The total geometric loss is only 20%. A monochromatic beam of tender X-rays can then be obtained, with a flux of the order of $1 \times 10^{12}$ photons $s^{-1}$ and a micro-beam size of approximately 7 µm (H) × 6 µm (V).

Crystal pairs of Si (220) can also be used to improve the energy resolution. The energy resolution is a function of the Darwin width based on the crystal, and of the beam vertical divergence, which is determined by the slope error of the TM and the distance between the virtual source and the CM. Obviously, a larger slope error of the TM will decrease the energy resolution. However, even if the slope error of the TM is 1.5 µrad, the energy resolution at 7 keV will be 1.2 eV with Si (111) and 0.6 eV with Si (220) according to the *SHADOW*/*XOP* simulation, while the focus is approximately 7.5 µm (H) × 9 µm (V). This is acceptable for microscopic XAFS; thus the exact value of the slope error of TM is not crucial if in the range 1.0–1.5 µrad.

### 3.3. Thermal load and harmonic suppression

To obtain high-quality XAFS spectra, it is important to reduce the number of higher harmonic photons. We use a CM mirror as the harmonic rejection mirror, with a coating of $B_4C$ and Ni. The reflectivity of the two coatings is shown in Fig. 5.

CHKB is not used as the high-order suppressor because the mirror for suppressing harmonics absorbs heat. A downstream mirror can achieve a much lower power density. In this project, the total power from the source is about 280 W, and approximately 252 W is absorbed by the TM mirror with a maximum power density of 8.3 mW $mm^{-2}$. Finite-element analysis shows that thermal deformation will cause a long-period slope error that should be partially compensated for by a proper bender.

Only a power of 28 W will be delivered to the virtual source. However, since the distance from the virtual source to CHKB is so short, the maximum power density on CHKB will reach 0.28 W $mm^{-2}$ even with a fairly low power of 3 W. The CM mirror with a $B_4C$ coating absorbs 12 W, and the maximum power density on CM is approximately 0.3 W $mm^{-2}$. After these mirrors, the heat load on a crystal is approximately 13 W or 23 W, depending on the coating of the CM mirror. The maximum power density on the first crystal is approximately 7.5 W $mm^{-2}$, which is so high that the monochromator should be cooled by liquid nitrogen.

To summarize, the power imposed on all optical elements is nearly constant, and the slope error comes from thermal deformation that can be maintained, controlled or compen-

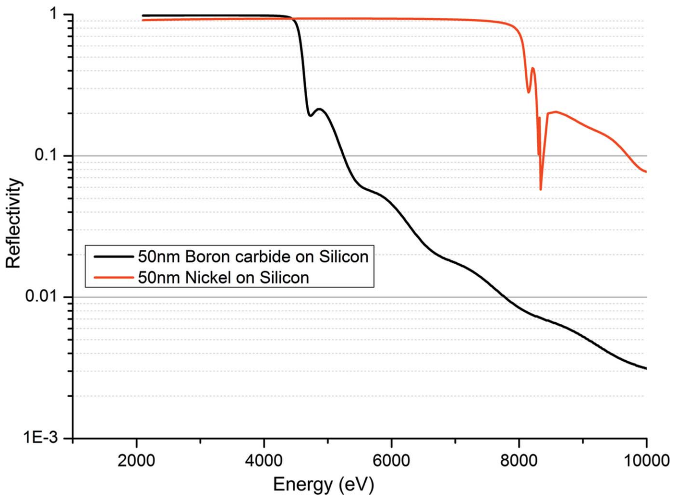

**Figure 5**
Reflectivity curve of $B_4C$ and Ni with an incidence angle of 7 mrad.

sated for, as long as the power is not too high. Therefore, compared with an undulator beamline, which either works under the tapered mode (Caliebe *et al.*, 2019) at the expense of flux or under the gap-scanning mode (Welter *et al.*, 2019) at the expense of speed, a bending-magnet beamline can provide better performance in terms of thermal stability and reliability, which can be the most powerful advantage in energy scanning applications, as long as there is sufficient flux.

## 4. Endstations

There will be two XAFS stations at this beamline, one a conventional XAFS station for bulk (~mm)-size samples and the other a microscopic XAFS station for micrometric particles and inhomogeneous samples. A schematic of the experimental setup is shown in Fig. 6.

The large beam directly behind the monochromator will be used for conventional XAFS. Either transmission X-rays, fluorescence or photoelectrons can be used as diagnostic signals to obtain an XAFS spectrum. Samples and a fluorescent detector will both work under a vacuum or helium environment. Additional details about conventional XAFS stations can be found in the literature (Xiao *et al.*, 2017; Zheng *et al.*, 2014); we describe only the performance associated with the beamline design here.

Due to the short distance between the monochromator and sample, the beam on the sample can be very stable. For example, the vertical displacement of the beam ($\Delta h$) is a function of the double crystals' detuning angle ($\Delta\theta_{\rm pitch}$) and of the distance between the monochromator and sample (~3 m), as described by

$$\Delta h = d\Delta\theta_{\rm pitch}.$$

Despite a pitch drift of 50 µrad at worst during energy scanning, the vertical position of the beam only drifts 150 µm, which is negligible compared with the beam size of 2.4 mm (V). As a result, quick-XAFS has a huge advantage, and its speed will only be restricted by the manufacturer. A KOHZU double-cam fixed-exit monochromator (double-cam DCM) (Caliebe *et al.*, 2006), which has been demonstrated at a number of other beamlines (Prestipino *et al.*, 2011), can be used for quick-XAFS.

Quick-XAFS is also important in scanning micro-XAFS for an acceptable collection time, and it has a similar advantage here. Since KB follows a collimating beam, the displacement of focus will not be amplified by the distance between the monochromator and KB. The vertical displacement ($\Delta h$), which is the product of the angle drift ($\Delta\theta_{\rm pitch}$) caused by the monochromator and the distance (0.25 m) between the sample and KB, will influence the position of focus. Even a drift of 2 µrad will result in a vertical displacement of only 0.5 µm. This value is not large, and can be handled by feedback systems (Barrea *et al.*, 2010; Fischetti *et al.*, 2004; van Silfhout *et al.*, 2014).

In addition to the scanning micro-XAFS discussed above, full-field nano-XAFS also can be used at the same position, but it only works under transmission mode. Full-field nano-XAFS is based on zone-plate TXM, whose details can be found in the literature (Meirer *et al.*, 2011).

In the case of this beamline, the divergence of the focus achieved by KB is well matched to the objective lens, which is a zone plate. As a result, an extra condenser is not necessary, saving much flux for TXM and full-field nano-XAFS (Meirer *et al.*, 2011). Although full-field nano-XAFS can work in any TXM beamline, only a TXM beamline with sufficient flux and fewer energy-dependent optical elements can make full-field nano-XAFS more practical.

In contrast to scanning micro-XAFS, TXM-related applications do not usually require a stabilized beam on the sample. Conversely, a rapid wobbling beam (Rau *et al.*, 2006), which increases the FOV and blurs the illumination, may sometimes be better. In the case of this beamline, *SHADOW*/*XOP* analysis shows that a pitch drift of 5 µrad caused by the monochromator will cause an intensity fluctuation of 3.5% at an energy of 7 keV with Si (111); the energy drift can be ignored, whereas the positional drift of focal beam is 1.25 µm. Thus, the second crystal can be cyclically scanned at a high frequency to obtain a relatively uniform illumination that can be helpful to full-field applications.

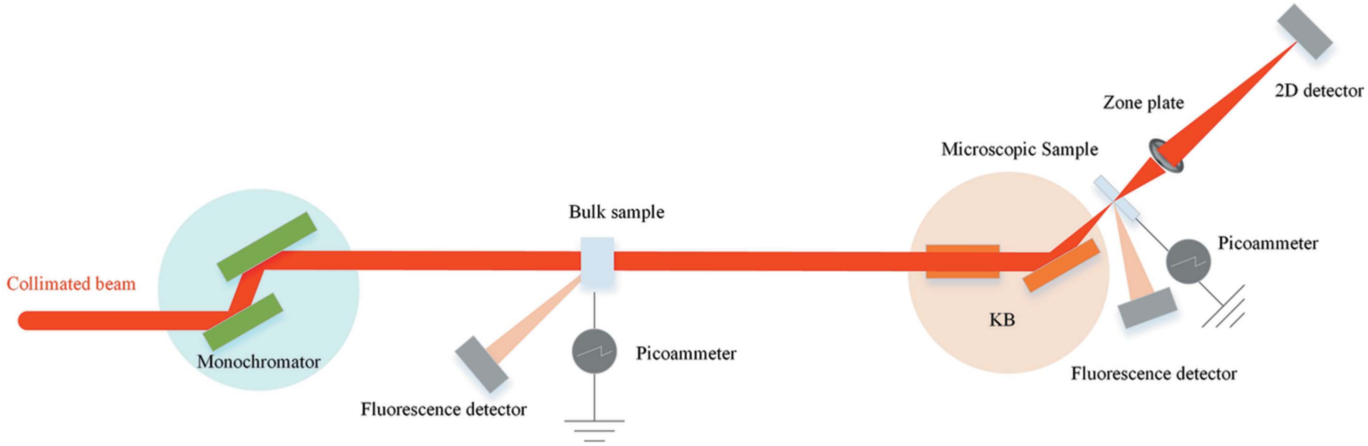

**Figure 6**
Side-view schematic of the endstations.

## 5. Prospect of such design at HEPS

A similar optical design can be used for the hard X-ray region. A coating of Pt or 15 nm $B_4C$ on Pt, with the same incidence angle of 7 mrad as in the current case, can be used to extend the energy to 11 keV, especially for experiments such as zone-plate-based TXM and TXM-based nano-XAFS. Moreover, of course, an increased energy range can be valuable (Andrews & Weckhuysen, 2013).

Even if we are not considering TXM-related applications, a micro-scale beam based on a bending magnet still has value that cannot be ignored, especially at HEPS. Using a similar design, the energy range can be extended to hard X-rays. For the energy range from 4.5 keV to 21 keV, there should be some difference in the optical parameters from the current case, mainly due to the cutoff incidence angle of the coating. An Rh coating with an incidence angle of 3 mrad would be useful for 4.5 keV–21 keV, and the acceptance of the source would be approximately 0.8 mrad (H) × 0.085 mrad (V). A flux of more than $5 \times 10^{11}$ photons $s^{-1}$ could easily be obtained in almost the whole energy range from 4.5 keV to 21 keV, and a micrometre beam size is not a problem. If a Pt coating with an incidence angle of 2 mrad can be used for the energy range 15–40 keV, then the flux at the micrometre station will be approximately $2 \times 10^{11}$ photons $s^{-1}$.

To achieve higher flux and better energy resolution, especially for energies above 10 keV when the diffraction efficiency of the crystal based on polarization has little influence, a horizontal monochromator is useful according to the size of the virtual source, which is 17 µm (H) × 170 µm (V) at HEPS. With a horizontal monochromator, the slope error of TM will have less influence on the energy resolution. Therefore, a relatively cost-effective longer mirror, such as a 1350 mm clear aperture mirror with a tangential slope error of 2 µrad could be used as the TM and would be helpful for the flux. Furthermore, an elliptical cylindrical mirror could be used instead of the CM and VKB, reducing the number of mirrors and adding flux. Finally, in the case of 15–40 keV, the flux at the micrometre station could be approximately $5 \times 10^{11}$ photons $s^{-1}$ at 20 keV and $2.5 \times 10^{11}$ photons $s^{-1}$ at 40 keV, with a focus size of approximately 10 µm × 10 µm. Crystal pairs of Si (111) are used in all the above cases.

## 6. Conclusions

This paper describes a bending-magnet beamline design based on the diffraction-limited lattice design of HEPS, for the purposes of micro-focusing and high-flux throughput.

In the case presented here, a beamline for tender X-ray XAFS applications, which is included in the first phase of HEPS, is designed to cover the energy range from 2.1 keV to 7.8 keV. There will be two XAFS stations at this beamline, a conventional XAFS station for bulk (∼mm)-size samples and a microscopic XAFS station for particles and inhomogeneous samples. With a proper micrometre spot size and divergence, scanning micro-XAFS with a resolution of 7 µm (H) × 6 µm (V) and TXM-based nano-XAFS with a resolution of approximately 30 nm can be enabled at the same position of focus with flux of the order of $1 \times 10^{12}$ photons $s^{-1}$.

If this beamline functions well as engineered and its desired performance is realized, more bending-magnet beamlines will be built in Phase II using a similar design structure for various scientific objectives.

## Acknowledgements

We thank LetPub (www.letpub.com) for its linguistic assistance during the preparation of this manuscript.

## Funding information

This work was supported by the National Natural Science Foundation of China (grant No. 11475213).

## References

Andrews, J. C., Brennan, S., Pianetta, P., Ishii, H., Gelb, J., Feser, M., Rudati, J., Tkachuk, A. & Yun, W. (2009). *J. Phys. Conf. Ser.* **186**, 012002.

Andrews, J. C. & Weckhuysen, B. M. (2013). *ChemPhysChem*, **14**, 3655–3666.

Barrea, R. A., Gore, D., Kujala, N., Karanfil, C., Kozyrenko, S., Heurich, R., Vukonich, M., Huang, R., Paunesku, T., Woloschak, G. & Irving, T. C. (2010). *J. Synchrotron Rad.* **17**, 522–529.

Barrea, R. A., Huang, R., Cornaby, S., Bilderback, D. H. & Irving, T. C. (2009). *J. Synchrotron Rad.* **16**, 76–82.

Caliebe, A. W., Murzin, V., Kalinko, A. & Görlitz, M. (2019). *AIP Conf. Proc.* **2054**, 060031.

Caliebe, W. A., So, I., Lenhard, A. & Siddons, D. P. (2006). *Radiat. Phys. Chem.* **75**, 1962–1965.

Canestrari, N., Karkoulis, D. & del Rio, M. S. (2011). *Proc. SPIE*, **8141**, 814112.

Falcone, R., Jacobsen, C., Kirz, J., Marchesini, S., Shapiro, D. & Spence, J. (2011). *Contemp. Phys.* **52**, 293–318.

Fischetti, R., Stepanov, S., Rosenbaum, G., Barrea, R., Black, E., Gore, D., Heurich, R., Kondrashkina, E., Kropf, A. J., Wang, S., Zhang, K., Irving, T. C. & Bunker, G. B. (2004). *J. Synchrotron Rad.* **11**, 399–405.

Guttmann, P., Bittencourt, C., Rehbein, S., Umek, P., Ke, X. X., Van Tendeloo, G., Ewels, C. P. & Schneider, G. (2012). *Nat. Photon.* **6**, 25–29.

Huebner, S., Miyakawa, N., Kapser, S., Pahlke, A. & Kreupl, F. (2015*a*). *IEEE Trans. Nucl. Sci.* **62**, 588–593.

Huebner, S., Miyakawa, N., Pahlke, A. & Kreupl, F. (2015*b*). *Phys. Status Solidi B*, **252**, 2564–2573.

Jefimovs, K., Vila-Comamala, J., Stampanoni, M., Kaulich, B. & David, C. (2008). *J. Synchrotron Rad.* **15**, 106–108.

Jiao, Y., Xu, G., Cui, X.-H., Duan, Z., Guo, Y.-Y., He, P., Ji, D.-H., Li, J.-Y., Li, X.-Y., Meng, C., Peng, Y.-M., Tian, S.-K., Wang, J.-Q., Wang, N., Wei, Y.-Y., Xu, H.-S., Yan, F., Yu, C.-H., Zhao, Y.-L. & Qin, Q. (2018). *J. Synchrotron Rad.* **25**, 1611–1618.

Juanhuix, J., Gil-Ortiz, F., Cuní, G., Colldelram, C., Nicolás, J., Lidón, J., Boter, E., Ruget, C., Ferrer, S. & Benach, J. (2014). *J. Synchrotron Rad.* **21**, 679–689.

Lee, W. K., Reininger, R., Loo, W., Gambella, R., O'Hara, S., Chu, Y. S., Zhong, Z. & Wang, J. (2015). *Proc. SPIE*, **9592**, 959209.

Marcus, M. A., MacDowell, A. A., Celestre, R., Manceau, A., Miller, T., Padmore, H. A. & Sublett, R. E. (2004). *J. Synchrotron Rad.* **11**, 239–247.

Meirer, F., Cabana, J., Liu, Y., Mehta, A., Andrews, J. C. & Pianetta, P. (2011). *J. Synchrotron Rad.* **18**, 773–781.

Meirer, F. & Weckhuysen, B. M. (2018). *Nat. Rev. Mater.* **3**, 324–340.

Moreno, T., Belkhou, R., Cauchon, G., Idir, M. & Mercere, P. (2006). *AIP Conf. Proc.* **879**, 455–458.

Prestipino, C., Mathon, O., Hino, R., Beteva, A. & Pascarelli, S. (2011). *J. Synchrotron Rad.* **18**, 176–182.

Rau, C., Crecea, V., Richter, C. P., Peterson, K. M., Jemian, P. R., Neuhausler, U., Schneider, G., Yu, X., Braun, P. V., Chiang, T. C. & Robinson, I. K. (2006). *Proc. SPIE*, **6318**, 63181G.

Silfhout, R. van, Kachatkou, A., Groppo, E., Lamberti, C. & Bras, W. (2014). *J. Synchrotron Rad.* **21**, 401–408.

Silversmit, G., Vekemans, B., Nikitenko, S., Bras, W., Czhech, V., Zaray, G., Szaloki, I. & Vincze, L. (2009). *J. Synchrotron Rad.* **16**, 237–246.

Tanaka, T. & Kitamura, H. (2001). *J. Synchrotron Rad.* **8**, 1221–1228.

Tian, Y. C., Li, W. J., Chen, J., Liu, L. H., Liu, G., Tkachuk, A., Tian, J. P., Xiong, Y., Gelb, J., Hsu, G. & Yun, W. B. (2008). *Rev. Sci. Instrum.* **79**, 103708.

Vila-Comamala, J., Pan, Y., Lombardo, J., Harris, W. M., Chiu, W. K., David, C. & Wang, Y. (2012). *J. Synchrotron Rad.* **19**, 705–709.

Wang, Y. D., Ren, Y. Q., Zhou, G. Z., Du, G. H., Xie, H. L., Deng, B. & Xiao, T. Q. (2018). *Nucl. Instrum. Methods Phys. Res. A*, **896**, 108–112.

Welter, E. (2012). *J. Synchrotron Rad.* **19**, 905–910.

Welter, E., Chernikov, R., Herrmann, M. & Nemausat, R. (2019). *AIP Conf. Proc.* **2054**, 060031.

Winarski, R. P., Holt, M. V., Rose, V., Fuesz, P., Carbaugh, D., Benson, C., Shu, D., Kline, D., Stephenson, G. B., McNulty, I. & Maser, J. (2012). *J. Synchrotron Rad.* **19**, 1056–1060.

Xiao, Q., Maclennan, A., Hu, Y., Hackett, M., Leinweber, P. & Sham, T.-K. (2017). *J. Synchrotron Rad.* **24**, 333–337.

Yashchuk, V. V., Morrison, G. Y., Marcus, M. A., Domning, E. E., Merthe, D. J., Salmassi, F. & Smith, B. V. (2015). *J. Synchrotron Rad.* **22**, 666–674.

Yuan, Q., Zhang, K., Hong, Y., Huang, W., Gao, K., Wang, Z., Zhu, P., Gelb, J., Tkachuk, A., Hornberger, B., Feser, M., Yun, W. & Wu, Z. (2012). *J. Synchrotron Rad.* **19**, 1021–1028.

Zheng, L., Zhao, Y. D., Tang, K., Ma, C. Y., Hong, C. H., Han, Y., Cui, M. Q. & Guo, Z. Y. (2014). *At. Spectrosc.* **101**, 1–5.